



Structural tale of two novel (Cr, Mn)C carbides in steel

G.K. Tirumalasetty^{a,b,*}, C.M. Fang^c, J. Jansen^a, T. Yokosawa^{a,d}, M.F.J. Boeije^e,
J. Sietsma^f, M.A. van Huis^{a,c}, H.W. Zandbergen^a

^a Kavli Institute of Nanoscience, Delft University of Technology, Lorentzweg 1, 2628 CJ Delft, The Netherlands

^b Materials Science Center, The University of Manchester, Grosvenor Street, Manchester M17 HS, UK

^c Soft Condensed Matter, Debye Institute for Nanomaterials Science, Utrecht University, Princetonplein 5, 3584 CC Utrecht, The Netherlands

^d Institute for Nuclear Waste Disposal, Karlsruhe Institute of Technology, Hermann-von-Helmholtz-Platz 1, D-76344 Eggenstein-Leopoldshafen, Germany

^e Fundamental Aspects of Materials and Energy, Faculty of Applied Sciences, Delft University of Technology, Mekelweg 15, 2629 JB Delft, The Netherlands

^f Department of Materials Science and Engineering, Delft University of Technology, Mekelweg 2, 2628 CD Delft, The Netherlands

Received 12 May 2014; received in revised form 13 June 2014; accepted 14 June 2014

Available online 16 July 2014

Abstract

Chromium (Cr), manganese (Mn) and carbon (C) are well known alloying elements used in technologically important alloy steels and advanced high strength steels. It is known that binary CrC_x and MnC_x carbides can be formed in steels, but in this study we reveal for the first time that Cr and Mn were found combined in novel ternary cementite type (Cr, Mn)C carbides. Electron diffraction experiments showed that Cr, Mn and C formed two distinct carbide phases possessing orthorhombic and monoclinic crystal structures. Density functional theory calculations were performed on these phases and excellent agreement was found between calculations and experiments on the lattice parameters and relative atomic positions. The calculations showed that the combination of Mn and Cr resulted in a very high thermodynamic stability of the (Cr, Mn)C carbides, and that local structural relaxations are associated with carbon additions. Possible implications of these ternary carbides for novel applications in steel design and manufacturing are discussed.

© 2014 Acta Materialia Inc. Published by Elsevier Ltd. All rights reserved.

Keywords: (Cr, Mn)C carbides; Steel; Transmission electron microscopy; Electron diffraction; First principles calculations

1. Introduction

Soaring fuel costs, increased environmental concerns and improved safety regulations have fostered the demand for stronger and tougher materials in the automotive, shipping, military, chemical and aerospace industries. Multi-phase (MP) steels exhibiting the transformation-induced plasticity (TRIP) effect have raised much interest in recent years for providing a good balance of strength and ductility

[1–5]. In addition to mechanical strength and formability, improved hardenability and wear resistance contribute towards the overall performance of the steel. The most effective way of enhancing the hardenability is achieved by the addition of chromium [6]. Chromium (Cr) in steels acts as a ferrite stabilizer and helps in expanding the ferrite region in the phase diagram. Furthermore, it also has a tendency to combine with carbon (C) in iron to form carbides. The Cr atoms in low alloyed steels are found to replace Fe atoms in Fe_3C to produce $(\text{Fe, Cr})_3\text{C}$ carbides [7]. Manganese (Mn) on the other hand has a high tendency to dissolve in α -Fe (ferrite). Nonetheless, manganese can also form carbides in steel, and this usually enters cementite (Fe_3C) as $(\text{Fe, Mn})_3\text{C}$ [7]. However, carbides in steels that contain both Cr and Mn have not been reported previously.

* Corresponding author at: Materials Science Center, The University of Manchester, Grosvenor Street, Manchester M17 HS, UK. Tel.: +44 161 3063588.

E-mail address: ganesh.tirumalasetty@manchester.ac.uk (G.K. Tirumalasetty).

The Cr–Mn–C bulk phase system was investigated previously by Schuster and Nowotny [8]. Schatt [9] explained that Cr and Mn could mutually substitute one another and can form $(\text{Cr}, \text{Mn})_{23}\text{C}_6$ and $(\text{Cr}, \text{Mn})_7\text{C}_3$ types of carbides. Thermodynamic evaluation of the Fe–Cr–Mn–C system was also carried out by Lee [10] and the expected carbide phases in this system were reported, but not cementite type carbides involving both Cr and Mn. The known carbides with Cr and Mn are listed in Table 1 [11–18]. In this study, we report on the structure and chemical composition of two new ternary cementite type $(\text{Cr}, \text{Mn})\text{C}$ carbides found in multiphase steel using transmission electron microscopy (TEM) and using quantum mechanical density functional theory (DFT) calculations.

2. Experiments and methods

2.1. Material and sample preparation

The chemical composition (wt.%) of the multiphase steel used in the present work is given in Table 2. The material is produced on an industrial hot dip galvanizing line using an intercritical annealing cycle, which is used generally for dual phase (DP) and TRIP steels. The specimens for TEM investigation were initially ground along the normal direction (ND)–transverse direction (TD) plane using SiC paper with roughness from 350 down to 4000 grit. Electro-polishing was carried out on the ground samples in a twin-jet polisher using freshly prepared electrolyte having composition of 100 ml perchloric acid, 300 ml butanol and 500 ml methanol maintained at a temperature of -20°C .

2.2. TEM experimental details

TEM analysis was carried out using CM 300T and CM 200 transmission electron microscopes operating at 300 kV and 200 kV to identify the microstructures and carbides. Energy dispersive X-ray spectroscopy was employed to investigate the chemical compositions of carbide phases. Selected area electron diffraction (SAED), convergent beam electron diffraction (CBED) and nanobeam electron diffraction (NBED) were employed to study the carbides

in this steel and the orientations of the diffraction patterns were defined with respect to the electron beam. Both SAD and CBED are carried out with 300T while NBED is carried out using a CM 200 microscope. In SAED, a parallel beam of electrons is incident on the specimen, with the specimen field selected using a sub-specimen image-plane aperture. In CBED the electron beam is converged in the form of a cone focused onto the specimen. In principle, with this technique, one can perform a diffraction experiment over several incident angles simultaneously. Thereby it can reveal the full three-dimensional symmetry of a crystal. NBED is a technique used to observe a diffraction pattern with sharp spots by using a narrow parallel electron beam illuminating a specimen area of about a few tens of nanometers in diameter.

For unit cell reconstruction using SAED and for CBED analysis, carbides located at the edge of grains (as shown in Fig. 1b and c) were chosen in order to reduce contributing reflections from the matrix. For the NBED work, several smaller sized carbides located at the edge of grains as shown in Fig. 1b and c were selected and were tilted to zone axis. All the diffraction patterns were recorded at room temperature on thin areas typically 10–40 nm thick found at the edges of the carbides. For the diffraction experiments a small spot size (5–10 nm) was used with exposure times of 10–20 s. After each recording of a diffraction pattern, the specimens were cleaned using plasma cleaner in order to prevent carbon contamination rings in the diffraction patterns.

2.3. Multislice least square (MSLS) refinements

The structure refinements were performed on several data sets of digitally recorded NBED patterns using the MSLS refinement computer program package [19,20]. Given that the diffraction patterns contain only two-dimensional (2-D) data, a right zone axis was entered manually so as to convert the 2-D indices to the correct indices of the reflections. The intensity of each reflection is then integrated individually by the software and for every reflection, and the background level is subtracted. The intensity which is directly surrounding the reflection is taken as an estimate for the background intensity. MSLS software uses the resulting intensity data to perform a least-squares refinement of crystal structure

Table 1
List of known phases and structures with Cr, Mn and C.

Phase	Space group (number)	Lattice parameter a (Å)	Lattice parameter b (Å)	Lattice parameter c (Å)	α (°)	β (°)	γ (°)
$(\text{Cr}, \text{Mn})_7\text{C}_3$ [10]	$Pnma$ (62)	4.54	6.95	11.97	90	90	90
$(\text{Cr}, \text{Mn})_7\text{C}_3$ [7]	$P63mc$ (186)	13.96	13.96	4.53	90	90	120
$(\text{Cr}, \text{Mn})_{23}\text{C}_6$ [7,11]	$Fm-3m$ (225)	10.65	10.65	10.65	90	90	90
Cr_3C [12]	$Pnma$ (62)	5.12	6.8	4.58	90	90	90
CrC [13]	$Fm-3m$ (225)	4.03	4.03	4.03	90	90	90
Cr_3C_2 [13]	$Cmcm$ (63)	2.85	9.25	6.96	90	90	90
Cr_3C_2 [14]	$Pnma$ (62)	5.53	2.83	11.49	90	90	90
Mn_5C_2 [15]	$C12/c1$ (15)	11.67	4.58	5.09	90	97.71	90
Mn_3C [16]	$Pnma$ (62)	5.12	6.8	4.58	90	90	90
$\text{MnC}_{0.07}$ [17]	$I4-3m$ (217)	8.97	8.97	8.97	90	90	90
$\text{Mn}_{3.6}\text{C}_{0.4}$ [17]	$Fm-3m$ (225)	3.73	3.73	3.73	90	90	90

Table 2
Chemical composition (wt.%) of multi phase TRIP-assisted steel.

C	Mn	Si	Al	Cr	Nb	V	Ti	Ni	Cu	P	S	N
0.149	2.061	0.392	0.620	0.515	0.022	0.004	0.006	0.024	0.017	0.011	0.002	<0.0001

Table 3
Nanobeam electron diffraction data used for the refinement of O-carbides using Model A in Table 4.

Data set No	Zone	Number of observed reflections	Thickness (Å)	Crystal misorientation			R-value (%)
				<i>h</i>	<i>k</i>	<i>l</i>	
<i>MSLS-Model A</i>							
1	[201]	148	371.1(17)	0.109(17)	0.002(11)	−0.022(3)	1.941
2	[102]	155	138.2(19)	0.048(9)	0.13(3)	−0.024(5)	4.138
3	[110]	249	462.9(19)	0.125(4)	−0.125(4)	−0.011(5)	6.518
4	[102]	127	138.7(13)	−0.180(9)	−0.03(3)	0.09(5)	9.305
5	[102]	103	134.3(19)	−0.08(10)	0.12(3)	0.040(5)	3.465
6	[100]	148	359.3(6)	0.00	−0.017(11)	−0.034(9)	4.596
7	[201]	131	372.2(14)	0.013(17)	−0.014(11)	−0.027(3)	1.936
8	[102]	160	139.0(12)	0.041(9)	0.18(3)	−0.020(4)	4.865
9	[210]	177	173.2(11)	0.317(9)	−0.635(17)	0.602(13)	7.461
10	[102]	124	133.6(16)	−0.080(10)	−0.1(3)	0.04(5)	3.406
11	[210]	186	196.4(13)	−0.145(8)	0.291(17)	−0.456(13)	8.539
12	[010]	227	209.5(8)	−0.087(17)	0.000000	−0.027(10)	4.799
13	[010]	263	209.9(3)	−0.082(17)	0.000000	−0.014(10)	3.974

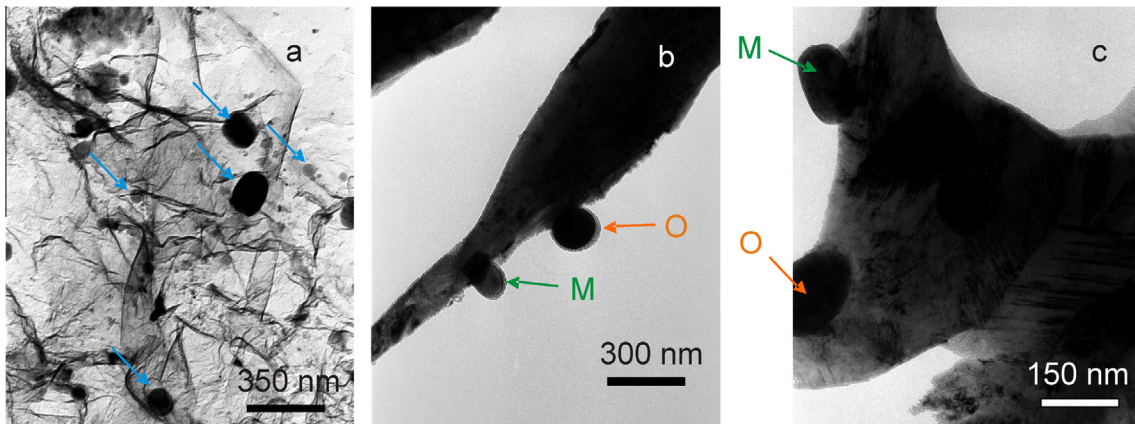


Fig. 1. (Cr,Mn)C carbides observed in multiphase steel: (a) spherical and elongated shaped carbides of various sizes in ferrite; (b) O- and M-carbides in ferrite; (c) O- and M-carbides in martensite.

parameters, based on a multislice algorithm taking dynamic scattering into account.

It is important to note that diffraction patterns from different zone axes and with different specimen thicknesses were used during the refinements, which is required for the refinement of the coordinates in three dimensions. Further, reflection intensities of the individual data sets cannot simply be combined into one data set, as the reflection intensities depend on specimen thickness and misorientations [21]. Therefore, for each of the (2-D) data sets, the specimen thickness and misorientation were refined individually. During refinements of thickness and misorientations, we have used the DFT coordinates as an initial model so as to minimize the risk that the iterative MSLS procedure becomes trapped in a local minimum. Thereafter atomic coordinates, the temperature factors and the occupancies are refined for the combined data. The *R* value was used as a measure of the correctness of the structure that is defined by

$$R = \frac{\sum_m (I_m^{obs} - I_m^{calc})^2}{\sum_m (I_m^{obs})^2} \quad (1)$$

here I_m^{obs} is the observed intensity of reflection *m* and I_m^{calc} is the corresponding calculated intensity of reflection *m*. In general, an *R* value of less than 6% suggests that the structure model is correct.

3. Results and discussion

3.1. TEM characterization

Carbides of Cr and Mn were observed in ferrite (body-centered cubic iron) and martensitic microstructures of the multiphase steel and were initially surveyed using bright field imaging in TEM. Fig. 1a shows carbides of (Cr,Mn)C found with various sizes, ranging between 60 nm and 300 nm. Energy dispersive spectrometry (EDS)

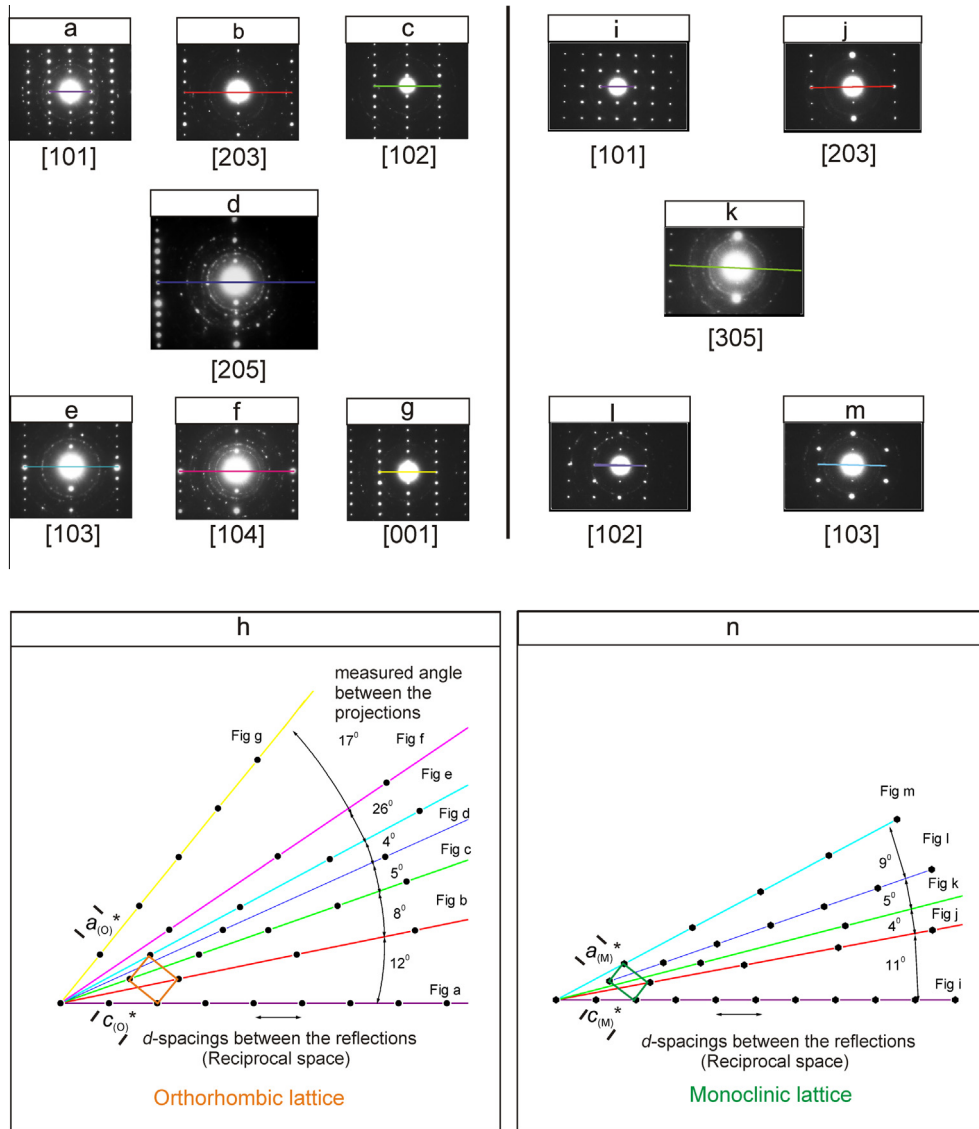


Fig. 2. (a–g, i–m) SAED patterns recorded from O and M-carbides by rotating about $b_{(O)}^*$ and $b_{(M)}^*$ axis. The coloured lines indicate the d -spacings of the reflections measured perpendicular to the constant rotation axis ($b_{(O)}^*$ and $b_{(M)}^*$). (h, n) Unit cell reconstruction with the reciprocal lattice points from the series of SAED patterns (in (a–g) and (i–m)) and with the angles between the projections. The cuboids show the unit cells of the carbides in reciprocal space. Here the symbols $a_{(O)}^*$, $b_{(O)}^*$, $c_{(O)}^*$, $a_{(M)}^*$, $b_{(M)}^*$, $c_{(M)}^*$ represent lattice parameters in reciprocal space of O- and M-carbides.

analysis was performed on several of these carbides to determine the chemical composition and the corresponding composition ratios of elements in the carbide. Interestingly, two carbides with different Mn/Cr ratios were identified possessing orthorhombic (O-carbide) and monoclinic (M-carbide) crystal structures in ferrite and martensitic grains as shown in Fig. 1b and c. In contrast to the ferrite matrix having Mn (2.22 at.%), Cr (0.79 at.%) and remaining Fe, the O-carbide as shown in Fig. 1b exhibited higher concentrations of Mn (7.23 at.%) and Cr (3.07 at.%), while M-carbide as shown in Fig. 1b showed equi-atomic ratios of Mn (2.98 at.%) and Cr (2.68 at.%). Out of the measured 44 carbides, 40 were of O-type and the Mn/Cr atomic ratio of these carbides was 1.8 ± 0.4 . The remaining four were of M-type and had a Mn/Cr atomic ratio of 1.07 ± 0.03 .

The unit cells of these carbides were identified by tilt series reconstruction from electron diffraction patterns. A series of diffraction patterns were recorded by rotating the carbides about a constant $b_{(O)}^*$ and $b_{(M)}^*$ axis (where the symbols $a_{(O)}^*$, $b_{(O)}^*$, $c_{(O)}^*$, $a_{(M)}^*$, $b_{(M)}^*$, $c_{(M)}^*$ represent lattice parameters in reciprocal space of O- and M-carbides) and the diffraction patterns were imaged using SAED. A total of seven diffraction patterns were taken for O-carbide along this rotation axis, as shown in Fig. 2a–g and the unit cell of the carbide was then reconstructed from the projections and the angles between them. Fig. 2h shows the unit cell reconstruction in reciprocal space. It follows that these carbides have an orthorhombic lattice. The lattice parameters of the O-carbide in real space ($a_{(O)}$ and $c_{(O)}$) were calculated from [010] projection in Fig. 3a with respect

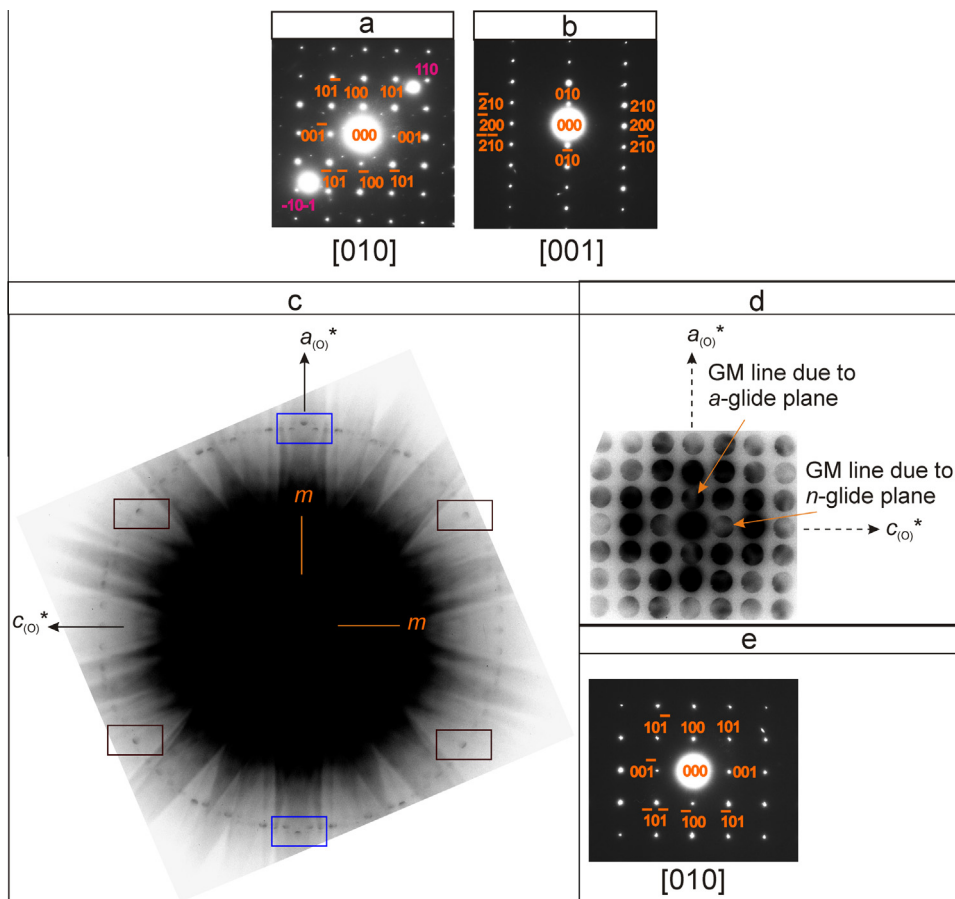


Fig. 3. (a) SAED pattern in [010] orientation of O-carbide along with 110 reflections of ferrite. (b) SAED pattern in [001] orientation of O-carbide. (c) CBED showing HOLZ of the carbide. From the brown and blue rectangles in (c), mirror (m) symmetry can be observed about $a_{(O)}^*$ and $c_{(O)}^*$ axes. (d) CBED showing ZOLZ of the carbide. GM line was seen about $a_{(O)}^*$ due to a glide plane and about $c_{(O)}^*$ due to n glide plane. (e) SAED pattern corresponding to CBED pattern in Fig. 3c and d. (For interpretation of the references to colour in this figure legend, the reader is referred to the online version of this article.)

to known d_{110} spacings of ferrite [22]. Lattice parameter ($b_{(O)}$) was calculated from [001] projection in Fig. 3b with ($a_{(O)}$) known from Fig. 3a. The unit cell parameters of the O-carbide were found to be $a_{(O)} = 5.09 \pm 0.05 \text{ \AA}$, $b_{(O)} = 6.98 \pm 0.05 \text{ \AA}$, $c_{(O)} = 4.55 \pm 0.05 \text{ \AA}$.

For the M-carbide, five diffraction patterns were recorded, as shown in Fig. 2i–m. The lattice parameters of the M-carbide in real space ($b_{(M)}$ and $c_{(M)}$) were calculated from [100] projection in Fig. 4a with respect to known d_{110} spacings of ferrite [22]. It follows that unit cell parameters of the carbide were $a_{(M)} = 6.83 \pm 0.05 \text{ \AA}$, $b_{(M)} = 4.54 \pm 0.05 \text{ \AA}$, $c_{(M)} = 5.00 \pm 0.05 \text{ \AA}$. The monoclinic angle $\beta_{(M)}$ is calculated by inserting the d spacings and the indices of several diffraction spots into a Rietveld refining procedure in powder diffraction software called Refcel [23] and it was found to be $\beta_{(M)} = 92.27^\circ$. Carbides of Cr or Mn with such a unit cell have not yet been reported (see Table 1 for the list of all Cr and Mn carbides reported in the literature). The space group of O-carbide and M-carbide was determined using convergent beam electron diffraction.

Fig. 3 shows the CBED pattern along the [010] zone axis of O-carbide. The point group of the carbide was determined from the higher order Laue zone (HOLZ) in Fig. 3c. This carbide showed a mirror (m) symmetry along $a_{(O)}^*$ and $c_{(O)}^*$ axis indicating mmm or $m2m$ point groups. Additionally, the space group of the O-carbide was determined from the zero order Laue zone (ZOLZ). The ZOLZ pattern in Fig. 3d showed an extinction rule with the Gjønnes–Moodie (GM) lines appearing in 100 and 001 diffraction disks. GM lines can appear within these disks if there is a screw axis or glide plane in the space group of the crystal. A glide plane in crystallography is a symmetry operation describing how a reflection in a plane, followed by a translation parallel with that plane, may leave the crystal unchanged. Glide planes are represented by a , b or c depending on which axis the glide is along. Further there is also the n glide, which is a glide along the half of a diagonal of a face of the unit cell. Screw axis symmetry is an operation describing how a combination of a rotation about an axis and a translation parallel to that axis leaves a crystal unchanged. Screw axes are represented by a

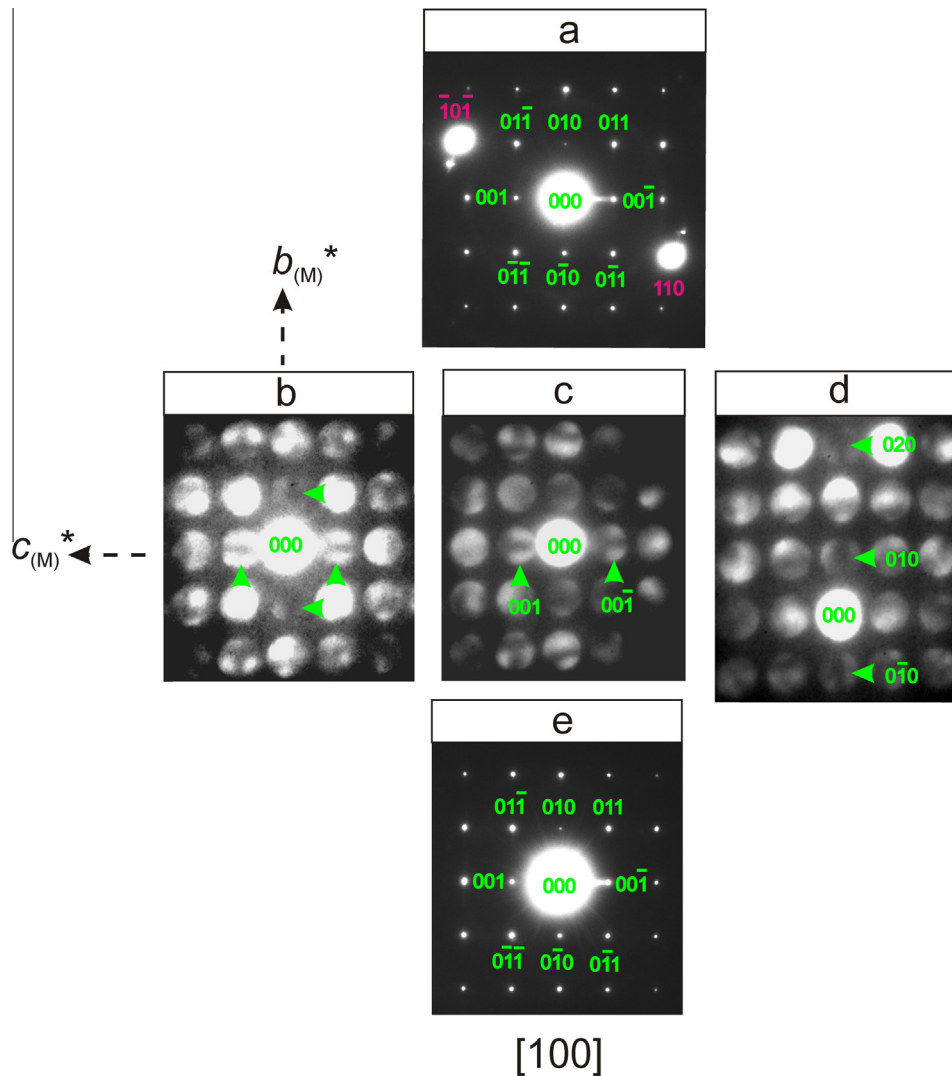


Fig. 4. (a) SAED pattern in [100] orientation of M-carbide along with 110 reflections of ferrite. (b) CBED showing ZOLZ of the carbide. GM line was seen about $b_{(M)}^*$ and $c_{(M)}^*$. The electron beam was tilted away from the [100] axis for observing the GM line clearly. (c) GM line about $c_{(M)}^*$ due to c glide plane; (d) GM line about $b_{(M)}^*$ due to 2_1 screw axis; (e) SAED pattern corresponding to CBED pattern in (b-d).

number, n , where the angle of rotation is $360^\circ/n$. The degree of translation is added as a subscript showing how far along the axis the translation is, as a portion of the parallel lattice vector. Intensity could be expected at the 100 and 001 diffraction disks and in the diffraction patterns because of the dynamical effects of electron diffraction. The possibility of a screw axis about $a_{(O)}^*$ or $b_{(O)}^*$ axis could

be eliminated based on the HOLZ pattern in Fig. 3c. The systematic absences for glide planes along the [010] direction were compared with the forbidden hkl diffraction spots for CBED analysis [24] and in the International Tables for Crystallography [25]. The comparisons indicate that the GM line along $a_{(O)}^*$ is observed due to a glide plane and the GM line along $c_{(O)}^*$ is observed due to a n glide plane

Table 4
MSLS-refined structural parameters of O-carbide.

Atomic coordinates	Wyckoff site	x	y	z	B	Occupation
<i>MSLS-Model A</i>						
Cr1	4c	0.0671 (4)	1/4	0.8255 (3)	0.065 (10)	1.0
Mn1	8d	0.1991 (5)	0.0897 (3)	0.3447 (2)	0.116 (5)	1.0
C1	4c	0.823 (3)	1/4	0.4648 (13)	0.42 (10)	1.0
C2	4a	0	0	0	0.1	0.238 (7)

Space group: $Pnma$, $a_{(O)} = 5.09 \text{ \AA}$, $b_{(O)} = 6.98 \text{ \AA}$, $c_{(O)} = 4.55 \text{ \AA}$, $\alpha = \beta = \gamma = 90^\circ$, $R = 5.06\%$. The temperature factor of C2 was set to 0.1, since the occupancy and temperature factor of an atom (in this case C2) are generally strongly coupled in the refinement.

as shown in Fig. 3c. The above results indicate that the O-carbide has the $Pnma$ space group.

Fig. 4b shows a ZOLZ CBED pattern taken with the [100] zone axis of an M-carbide. Dark lines are seen in the 010 and 001 reflection disks along $b_{(M)}^*$ and $c_{(M)}^*$ axes, respectively, as indicated by arrowheads. Although the lines are faint due to the larger sample thickness, the dark lines or the GM lines are formed by dynamical extinction rules. In order to verify this, the electron beam was tilted away from the [100] axis for observing the GM line more clearly, and to see the variation in intensities of forbidden reflections. Fig. 4c shows the GM line about $c_{(M)}^*$ and Fig. 4d shows the GM line about $b_{(M)}^*$. The GM lines along the $b_{(M)}^*$ and $c_{(M)}^*$ axes are formed by the extinction rules for 2_1 screw axis (2_1 is a 180° (twofold) rotation followed by a translation of $1/2$ of the lattice vector) along the $b_{(M)}^*$ axis ($0k0$: $k = 2n + 1$) and for c glide plane perpendicular to the $b_{(M)}^*$ axis ($00l$: $l = 2n + 1$), respectively [24]. The above results suggest that the space group of the M-carbide is $P2_1/c$.

Another five series of diffraction patterns were recorded along $a_{(O)}^*$, $b_{(O)}^*$ and $a_{(M)}^*$, $b_{(M)}^*$ axes to confirm the crystal lattice and the space group information of both O-carbide and M-carbide. The experimental diffraction patterns of all the diffraction recordings of these carbides were seen to be in good agreement with the simulated diffraction patterns generated from Crystal Kit software with the reconstructed lattice parameters and the obtained space group information. The newly found O-carbide has unit cell parameters and space group information that is similar to the well known cementite phase (Fe_3C), but with a larger $b_{(O)}$ axis in comparison to that of Fe_3C ($a_{(Fe_3C)} = 5.1 \text{ \AA}$, $b_{(Fe_3C)} = 6.77 \text{ \AA}$, $c_{(Fe_3C)} = 4.54 \text{ \AA}$) [26]. Furthermore, the lattice parameter of the M-carbide is related to the O-carbide as $a_{(M)} \approx b_{(O)}$, $b_{(M)} \approx c_{(O)}$, $c_{(M)} \approx a_{(O)}$ and with $P2_1/c$ space group being a maximal non-isomorphic subgroup (t -subgroup) [25][27] of $Pnma$ space group. It is important to note that t -subgroup is the maximal group which is formed from the parent group by retaining the translational elements, but the order of the point group is reduced [23,27].

3.2. MSLS models and refinements

Structure refinements were performed on several data sets of digitally recorded NBED patterns using the MSLS computer program package [19,20]. Since O-carbide had lattice parameters and space group similar to cementite structure (Fe_3C) [24] but an elongated b axis, interstitial positions were searched for additional C atom positions. Wyckoff sites for C at 4a position were found to be stable in this structure. Therefore, we performed refinements by assuming random distribution over three possible atomic arrangements by considering Cr and/or Mn metal atoms occupying the position of Fe at 4c and 8d sites and C atoms occupying 4c and 4a sites (Cr1 at 4c, Mn1 at 8d, C1 at 4c and C2 at 4a; Mn1 at 4c, Cr1 and Mn2 at 8d, C1 at 4c and

C2 at 4a; Cr1 and Mn1 at 4c, Cr2 and Mn2 at 8d, C1 at 4c and C2 at 4a). The refined atomic coordinates, temperature factors and occupancies of these models are given in Table 4 (Model A) and Table S.2 (Models B and C) of the supplementary information (SI). In the case of M-carbide, which is related to O-carbide, Wyckoff sites for C at the 2a position were found to be stable in this structure. Therefore, we performed refinements by assuming random distribution over three possible atomic arrangements by considering Cr and/or Mn metal atoms occupying the 4e sites and C atoms occupying 4e and 2a sites (Cr1, Mn1, Cr2, Mn2, Cr3 at 4e, C1 at 4e and C2 at 2a; Mn1, Cr1, Mn1, Cr2, Mn2, Cr3, Mn3 at 4e, C1 at 4e and C2 at 2a; Cr1, Mn1, Cr2, Mn2, Mn3 at 4e, C1 at 4e and C2 at 2a). The refined atomic coordinates, temperature factors and occupancies of these models are given in Table 6 (Model C) and Table S.4 (Model A and Model B) of the SI. For the refinement of these models, the occupancy of some of the Cr and Mn sites was constrained, as it depends on the occupancy of C. For instance, in Table 4, Cr1 and Mn1 positions cannot be occupied simultaneously, so their combined occupancy was constrained to 1.

The data corresponding to individual electron diffraction patterns such as specimen thickness and misorientations corresponding to specific zone axis were refined individually for both O- and M-carbides as shown in Tables 3 and 5, S.1 and S.3 of SI. Thereafter atomic coordinates, the temperature factors and the occupancies were refined for the combined data and the results of the refinements are displayed in Tables 4 and 6, S.2 and S.4 of SI.

The average R value of all the data sets which gives the correctness of the structure was calculated for O-carbide and was found to be 5.06% for Model A, 5.28% for Model B and 5.07% for Model C, while the average R value for M-carbide was found to be 5.03% for Model A, 4.96% for Model B and 4.98% for Model C. An average R value of less than 6% suggests that all the refined models strongly agree with the experimental observations.

3.3. DFT calculations

In order to obtain more insight into the stability and crystal chemistry of O-carbide and M-carbide, DFT calculations were performed. This approach has been successfully applied to study the crystal structures and relative stability of iron carbides [28–31]. The code Vienna Ab-initio Simulation Package [32] was employed with the DFT within the projector-augmented wave method [33,34]. The generalized gradient approximation [35] was employed for the exchange and correlation energy terms [29]. The cut-off energy of the wave functions was 500 eV for the carbides. Reciprocal space integrations were carried out using a k -mesh of a $12 \times 10 \times 16$ grid (378 k -points) in the irreducible Brillouin zone (BZ) of θ - L_3X using the Monkhorst and Pack method [36]. That k -mesh is also used for the θ' - L_3X_{1+x} phases. Both the relative atomic positions and the shape and size of the simulation cell

Table 5
Nanobeam electron diffraction data used for the refinement of M-carbides using model C in Table 6.

Data set No	Zone	Number of observed reflections	Thickness (Å)	Crystal misorientation			R-value (%)
				<i>h</i>	<i>k</i>	<i>l</i>	
<i>MSLS-Model C</i>							
1	[100]	240	233.3(10)	0.000000	0.08(3)	0.013(9)	5.098
2	[100]	240	232.1(10)	0.000000	−0.04(3)	−0.003(9)	5.674
3	[201]	150	201.8(13)	0.008(3)	0.10(2)	−0.016(5)	3.835
4	[201]	143	214.9(11)	−0.034(4)	−0.871(16)	0.067(7)	7.389
5	[201]	172	157.(2)	0.318(11)	0.84(3)	−0.64(2)	3.081
6	[100]	233	226.7(11)	0.000000	0.18(3)	−0.020(10)	7.924
7	[100]	255	232.0(11)	0.000000	0.00(3)	0.053(10)	9.151
8	[201]	138	212.8(12)	0.052(3)	−0.685(15)	−0.104(6)	3.345
9	[201]	135	262.5(18)	−0.178(3)	−0.463(10)	0.357(6)	1.885
10	[100]	222	229.2(10)	0.000000	−0.02(3)	−0.030(9)	8.925
11	[100]	262	232.6(11)	0.000000	−0.22(3)	0.072(10)	8.071
12	[100]	242	232.2(10)	0.000000	−0.01(3)	0.056(9)	7.929
13	[203]	97	226.7(3)	0.023(3)	−0.310(13)	−0.015(19)	4.539
14	[203]	95	228.1(3)	0.011(3)	−0.336(11)	−0.007(18)	6.253
15	[203]	84	223.2(3)	−0.005(3)	−0.22(3)	0.003(20)	2.879
16	[203]	92	235.3(4)	−0.019(3)	0.440(8)	0.012(20)	6.740
17	[203]	90	231.3(3)	0.009(3)	0.321(11)	−0.005(18)	6.011
18	[203]	90	230.8(3)	0.026(3)	−0.376(10)	−0.017(19)	5.147
19	[203]	90	230.3(3)	−0.013(3)	0.295(14)	0.008(19)	5.617

Table 6
MSLS-refined structural parameters of M-carbide.

Atomic coordinates	Wyckoff site	<i>x</i>	<i>y</i>	<i>z</i>	<i>B</i>	Occupation
<i>MSLS-Model C</i>						
Mn1	4e	0.106(2)	0.3274(7)	0.1348(11)	0.1	0.25
Cr1	4e	0.106(2)*	0.3274(7)*	0.1348(11)*	0.1*	0.75*
Mn2	4e	0.4451(15)*	0.3722(5)*	0.1619(13)*	0.1*	0.25*
Cr2	4e	0.4451(15)	0.3722(5)	0.1619(13)	0.1	0.75
Mn3	4e	0.2598(9)	0.8484(6)	0.0183(14)	0.69(4)	1.0
C1	4e	0.288(3)	0.4527(20)	0.882(2)	1.9(2)	1.0
C2	2a	0	0	0	0.1	1.0

Space group: $P2_1/c$, $a_{(M)} = 6.83 \text{ \AA}$, $b_{(M)} = 4.54 \text{ \AA}$, $c_{(M)} = 5.00 \text{ \AA}$, $\alpha = \gamma = 90^\circ$, $\beta_{(M)} = 92.2^\circ$, $R = 4.98\%$. The temperature factor of Mn1, Cr2, C2 was set to 0.1, since the occupancy and temperature factor of an atom (in this case Mn1, Cr2, C2) are generally strongly coupled in the refinement. The * indicates the constraints used in the refinement procedure: $x(\text{Cr1}) = x(\text{Mn1})$, $y(\text{Cr1}) = y(\text{Mn1})$, $z(\text{Cr1}) = z(\text{Mn1})$, $x(\text{Mn2}) = x(\text{Cr2})$, $y(\text{Mn2}) = y(\text{Cr2})$, $z(\text{Mn2}) = z(\text{Cr2})$, $B(\text{Cr1}) = B(\text{Mn1})$, $B(\text{Mn2}) = B(\text{Cr2})$, $\text{Occ}(\text{Cr1}) = 1 - \text{Occ}(\text{Mn1})$, $\text{Occ}(\text{Mn2}) = 1 - \text{Occ}(\text{Cr2})$.

(the lattice parameters) were allowed to relax in order to find the lowest-energy state of each structure considered. All carbide phases were calculated as if they are bulk (periodic boundary conditions apply to all simulation cells), and therefore interface energies or other interactions with the Fe matrix are not taken into account in the calculated energies.

3.4. DFT-structure models

Based on the above-mentioned experimental results, we built structural models for the ternary MnCrC phases starting from the cementite phase, L_3C . The structure of L_3C as shown in Fig. 5a (where L is a metal (Fe) atom) consisting of a distorted hexagonal close packed (hcp)-type L sublattice was initially considered with C being inserted in the octahedral sites of ordered arrangements [29–31]. In the orthorhombic structure of L_3C , with space group

$Pnma$, there are three types of atoms at different Wyckoff sites: L1 at 8d, L2 at 4c and C1 at 4c, with two large unoccupied sites (4a and 4b). DFT calculations showed that carbon atoms (C2) prefer occupying one of the 4a sites where the energy difference is greater than 1 eV, which is in agreement with the structural optimizations as well as the work by Jiang for $\text{Fe}_3\text{C}_{1+x}$ [37]. Therefore, we used this configuration for the O carbide and corresponding structure model is given in Fig. 5b.

Regarding the M-carbide, there are three independent ways to add carbon atoms into the 4a sites: (a) two C atoms at positions (0,0,0) and (1/2,0,0); (b) the two C atoms at positions (0,0,0) and (0,1/2,1/2); and (c) the two C atoms occupy positions (0,0,0) and (1/2,1/2,1/2). The calculations showed that the configuration with two C atoms occupying (0,0,0) and (0,1/2,1/2) is much more stable than the other two with an energy difference of 0.9 eV per cell or 50 meV per atom. Therefore, we used this configuration

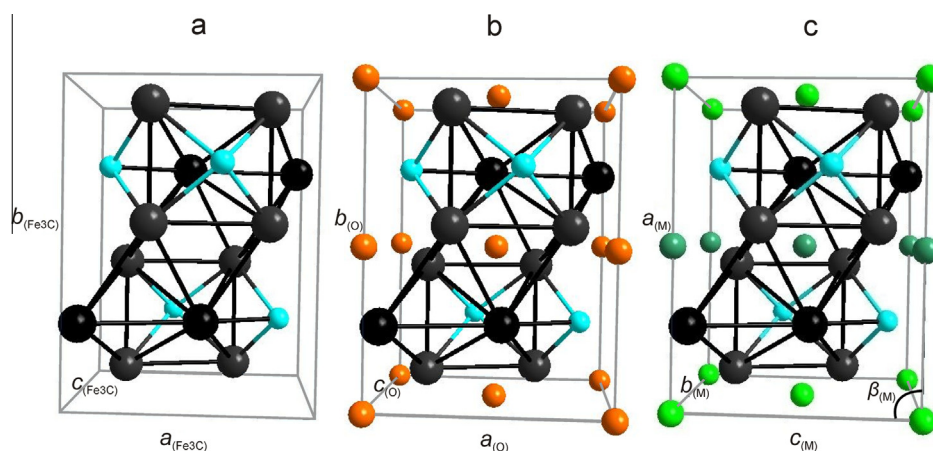


Fig. 5. Schematic structure showing the strong similarity between (a) the regular cementite Fe_3C structure, (b) the O-carbide and (c) the M-carbide with symmetries described in Table 7 and in the text. Large grey spheres in (a) and (b) represent L1 atoms at 8d Wyckoff sites and black spheres L2 atoms at 4c sites (here L is a metal atom: Fe, Cr or Mn). Small, sky blue spheres represent C1 atoms at 4c sites, and small orange spheres in (b) represent C2 positions at 4a sites. In panel (c), large grey spheres represent L1 atoms at 4e sites, black spheres L2 atoms at 4e sites, small sky blue spheres represent C1 atoms at 4e sites and light and dark green spheres represent C2 positions at 2a sites (C2 can occupy either two light green sites or two dark green sites). All the C atoms are positioned at octahedral sites of the distorted hcp-Fe sub-lattice. (For interpretation of the references to colour in this figure legend, the reader is referred to the online version of this article.)

for the m-carbide and the resultant structure model is given in Fig. 5c. The current configuration has a monoclinic lattice with a point symmetry of $2/m$ for $\text{L}_3\text{C}_{1.5}$ ($\text{L} = \text{Cr}, \text{Mn}$). Symmetry analysis showed that this C arrangement lowers the symmetry of the O-carbide with the space group from $Pnma$ to $P2_1/c$ with the lattice relationships:

$$a_{(M)} \approx b_{(O)}, \quad b_{(M)} \approx c_{(O)}, \quad c_{(M)} \approx a_{(O)}$$

and $\beta_{(M)}$ is the unique monoclinic angle between the $a_{(M)}$ and $c_{(M)}$ axes. The M-carbide has $\beta_{(M)}$ angles that deviate $\sim 2^\circ$ from 90° due to the occupation of the extra carbon atoms (C2). Nevertheless, at the atomic level, substitution of Mn, Cr and C atoms into L_3C structure results in a broken symmetry. However, our calculations show that the deviations of lattice parameters and coordinates of atoms from the monoclinic ones are not significant, since the averaged structure, obtained by TEM measurements, will be observed as orthorhombic and monoclinic. Therefore, we use $Pnma$ and $P2_1/c$ space groups in our discussion.

DFT calculations were performed for a binary chemical composition of L_3C_{1+x} ($\text{L} = \text{Cr}$ and Mn ; $x = 0, 0.25$) and ternary composition $(\text{Mn}_2\text{Cr})\text{C}_{1+x}$ ($x = 0, 0.25$) for comparison. The calculations showed that both Mn_3C and Cr_3C are stable relative to the elemental solids. The calculated lattice parameters showed a slight deviation from the experimental values of $\sim 3\%$. This might be due to difficulties in obtaining samples of high quality since Mn_3C is formed only at a very narrow temperature range of 1223–1323 K and Cr_3C is stable until 1023 K. Table S.5 of the SI further shows that the Mn/Cr alloying carbides have lower formation energies than the sum of the binary and that the energy differences of different Mn/Cr ordering for the Mn_2CrC phase are not significant. Nonetheless, it should be noted that Cr atoms occupy part of the 8d sites and the addition of one C atom at site 4a results in a broken symmetry of the orthorhombic lattices. However, the

calculations showed that the basic Mn/Cr sub-lattices remain orthorhombic.

As shown in Table 7, the addition of one C2 at the 4a site decreases the formation energies in most cases, except for the Model B of θ' - $\text{Mn}_2\text{CrC}_{1+x}$, which displays much lower formation energies. This indicates that the addition of C2 at one of the 4a sites causes Mn/Cr ordering with Cr atoms preferably occupying 8d sites. Certainly Cr/Mn alloying is possible, as shown in case of model C in Table 7, considering the contribution of configuration entropy at their high formation temperature. The calculations also show the impact of C2 addition and Mn/Cr ordering on the lattice parameters (models B and C in Table 7). The addition of one C2 at a 4a site increases the lattice parameters of the corresponding system. The largest deviation of the calculated lattice parameters is for the b -axis ($\sim -2.9\%$) for case B, while that deviation is only -0.3% for case A.

While comparing the DFT results with the experimental results as shown in Table 7, Tables S.8–S.9 of SI, we clearly see that all the three models for O-carbide show similar R values irrespective of the arrangement of atoms. However, Model A agrees best in terms of C occupation and lattice parameters. In the case of the M-carbide, all the three models show the same C occupation but Model C shows the best agreement in terms of lattice parameters and monoclinic angle ($\beta_{(M)}$).

3.5. Formation and stability of the M- and O-phases in steels

In order to understand the formation mechanism of the O- and M-phases, we assess their stability by the definition of formation energy (ΔE) as follows:

$$\Delta E = \{E(\text{L}_{n1}\text{L}_{n2}\text{C}_m) - [n_1E^{elem}(\text{L}_{n1}) + n_2E^{elem}(\text{L}_{n2}) + mE(\text{C})]\} / (n_1 + n_2 + m) \quad (2)$$

Table 7

Calculated lattice parameters and formation energies for O-carbide and M-carbide. $\Delta E = \{E(Ln_1Ln_2Cm) - [n_1 E^{elem}(Ln_1) + n_2 E^{elem}(Ln_2) + m E(C)]\} / (n_1 + n_2 + m)$ is the formation energy with respect to the elemental solids (bcc-Mn/Cr, graphite).

Compound	Atomic models	Atom	Wyckoff site	DFT-GGA Lattice parameters (Å)	Experimental		
					Lattice parameters (Å)	R-value	ΔE (meV) (atom)
O-carbide							
Mn ₂ CrC _{1.25}	A	Cr1	4c	$a = 5.03$ $b = 6.95$ $c = 4.52$	$a_{(O)} = 5.09$ $b_{(O)} = 6.98$ $c_{(O)} = 4.55$	5.06	−139.3
		Mn1	8d				
		C1	4c				
		C2	4a				
	B	Mn1	4c	$a = 5.07$ $b = 6.77$ $c = 4.56$		5.28	−124.7
		Mn2	8d				
		Cr1	8d				
		C1	4c				
	C	C2	4a	$a = 5.07$ $b = 6.83$ $c = 4.55$		5.07	−135.8
		Mn1	4c				
		Cr1	4c				
		Mn2	8d				
Mn _{1.5} Cr _{1.5} C _{1.5}	C	Cr2	8d	$a = 7.07$ $b = 4.64$ $c = 5.12$ $\beta = 92.0^\circ$	$a_{(M)} = 6.83$ $b_{(M)} = 4.54$ $c_{(M)} = 5.00$ $\beta_{(M)} = 92.2^\circ$	4.98	−134.5
		C1	4e				
		C2	2a				
		Mn1	4e				
		Cr1	4e				
		Mn2	4e				
	B	Cr2	4e	$a = 7.11$ $b = 4.60$ $c = 5.07$ $\beta = 91.2^\circ$		4.96	−134.5
		Mn3	4e				
		Cr3	4e				
		C1	4e				
		C2	2a				
		Mn1	4e				
A	Cr1	4e	$a = 7.12$ $b = 4.57$ $c = 5.06$ $\beta = 91.4^\circ$		5.03	−135.9	
	Mn2	4e					
	Cr2	4e					
	Cr3	4e					
	C1	4e					
	C2	2a					

ΔE is the formation energy with respect to the elemental solids (body centred cubic (bcc) Mn, bcc Cr and graphite) at 0 K and 0 Pa. It is also true that $\Delta E = \Delta H$ at 0 K and 0 Pa when the zero-vibration contribution is ignored.

Fig. 6 shows the stability of both O and M carbide phases as a function of formation energy with the formation energy of the cementite phase as a comparison. Clearly the both O and M carbides have similar stability at 0 K.

With the EDS analysis, minor contributions from Fe also appear in the experimental data for these carbides since the EDS signal in TEM comes not only from the precipitate but also from the matrix phase surrounding the precipitate, as a large part of the sample is hit by stray electrons. In addition, in general there is a contribution of the matrix material above and beneath the carbide [38]

below. Therefore, additional DFT calculations were carried out to check the possibilities of Fe in these carbide structures. We therefore performed DFT calculations on a series of systems which include Fe₃C_{1+x}, (Fe, L)₃C_{1+x} (L = Cr, Mn) and (Fe, Mn, Cr)₃C_{1+x} ($x = 1/4-1.0$).

The experimental EDS analysis of the O-type carbide showed ratios of Fe/Mn/Cr to be $\sim 22/2/1$. Therefore, we tested a composition of (Fe_{2.25/3}Mn_{0.50/3}Cr_{0.25/3})₃C_{1+x} ($x = 0-1.0$). Fe atoms occupy the 4c and 8d sites with Mn and Cr at 8d sites. The calculations for (Fe_{2.25/3}Mn_{0.50/3}Cr_{0.25/3})₃C_{1.25} showed that the formation energy of ~ 0.28 eV per unit cell or 0.070 eV per formula unit which is higher than the corresponding sum of the binary phases Fe₃C_{1.15}, Mn₃C_{1.25} and Cr₃C_{1.25} or the sum of the binary Fe₃C_{1.25} and the ternary (Mn_{2/3}Cr_{1/3})₃C_{1.25} as shown in

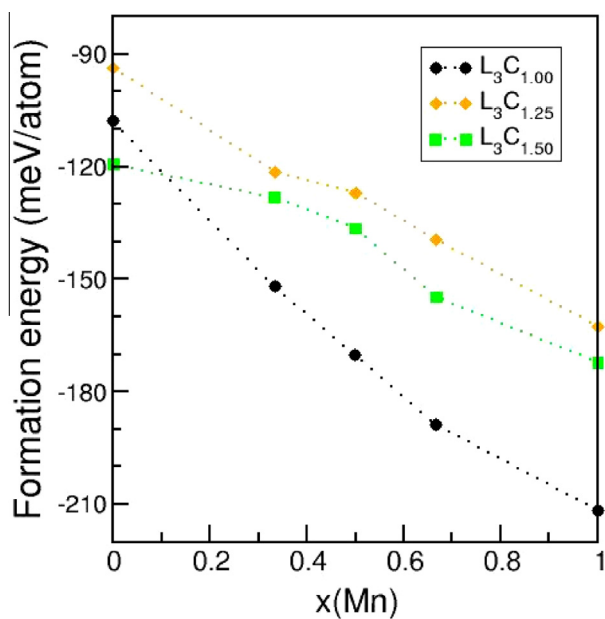


Fig. 6. Formation energy of the O- and M-carbide phases as a function of the Mn content x , whereby the chemical composition is given by the formula $[Mn_xCr_{(1-x)}]_3C_y$. The three curves are for different C concentrations ($y = 1.0, 1.25, 1.5$).

Table S.6 of SI. This clearly indicates that at thermal equilibrium conditions, the quaternary $(Fe_{2.25/3}Mn_{0.50/3}Cr_{0.25/3})_3C_{1.25}$ phase is energetically very unfavorable. For the monoclinic phase, two chemical compositions were tested. The calculations showed that high concentrations of Fe in the monoclinic phase have an additional energy cost of 0.82–0.95 eV per unit cell for the two chemical compositions as shown in Table S.7 of SI. This indicates instability of the Fe replacements in the M type carbide structure at 0 K.

As shown above, the first-principles calculations provided lattice parameters and coordination of atoms, in excellent agreement with the experimental observations. However, from the calculated formation energies, we cannot directly draw conclusions on the formation of the O- and M-phases. The DFT calculations are for the ground state at zero K, and entropy effects are neglected. Furthermore, the calculations also showed an interesting effect of extra C addition in the L_3C structure, such as magnetism for the $(MnCr)C_{1+x}$ phases, while their corresponding L_3C phase is non-magnetic. This is of importance because at elevated temperature magnetism has a strong impact on the free energy, as exemplified by the formation of austenite when heating ferrite [28,39]. Other factors, such as local chemical composition, thermal history, grain boundaries and interfaces and interface energies will also play a role in the formation of the carbide phases in steels at temperatures of typically 1300 K. Much more extensive experimental and computational studies are required to understand the formation of phases in the very rich, quaternary Fe–Mn–Cr–C system.

The novel ternary phases found in this work are interesting and of high importance for both science and industry. Elemental Cr as metal has a Mohs hardness of 8, which is just next to diamond in terms of hardness [40]. Furthermore, carbides of Cr are often very hard and are known to produce wear-resistant and corrosion-free surfaces. A uniform distribution of these newly formed carbides is more likely to enhance the hardness and wear resistance of these steels. We also performed calculations of the energy–volume relationship for the M-carbide and the data were processed with the Birch–Murnaghan relationship. Our results show a bulk modulus of ~ 225 GPa. The fitting also provided a large B'_0 value (9.8) as compared with normal materials (4–5). Therefore, these newly identified carbides offer many opportunities for developing novel applications.

4. Conclusions

Two novel ternary carbide phases, including both Cr and Mn, were identified in multiphase TRIP assisted steel. The carbides were characterized using TEM, electron diffraction and DFT calculations. Electron diffraction analysis revealed that the orthorhombic carbide possessed lattice parameters $a_{(O)} = 5.09$ Å, $b_{(O)} = 6.98$ Å, $c_{(O)} = 4.55$ Å, consistent with the $Pnma$ space group, while the monoclinic carbide possessed lattice parameters $a_{(M)} = 6.83$ Å, $b_{(M)} = 4.54$ Å, $c_{(M)} = 5.00$ Å, $\beta_{(M)} = 92.2^\circ$, consistent with the $P2_1/c$ space group. Atomic refinements with MSLS showed an average R value of less than 6% for both these structures with the DFT models strongly supporting the experimental observations. Remarkable Mn–Cr alloying leads to high thermodynamic stabilities of these ternary phases. Now that the presence of the novel carbides is disclosed, new steels may be designed whereby the size and concentration of the carbides are investigated to further improve steel performance.

Acknowledgement

The authors would like to thank Dr. D.N. Hanlon (Tata Steel RDT) for providing the samples and for useful discussions.

Appendix A. Supplementary data

Supplementary data associated with this article can be found, in the online version, at <http://dx.doi.org/10.1016/j.actamat.2014.06.035>.

References

- [1] Militzer M. *Science* 2002;298:975–6.
- [2] Tirumalasetty GK, van Huis MA, Fang CM, Xu Q, Tichelaar FD, Hanlon DN, et al. *Acta Mater* 2011;59:7406–15.
- [3] Tirumalasetty GK, van Huis MA, Kwakernaak C, Sietsma J, Sloof WG, Zandbergen HW. *Acta Mater* 2012;60:1311–21.
- [4] Tirumalasetty GK, van Huis MA, Kwakernaak C, Sietsma J, Sloof WG, Zandbergen HW. *Scripta Mater* 2014;71:29–32.

- [5] Tirumalasetty GK. Mechanics in steels through microscopy [PhD thesis]. ISBN: 9789077172902, 2013.
- [6] Suh DW, Park SJ, Han HN, Kim SJ. Metall Mater Trans A 2010;41(13):3276–81.
- [7] Smith WF. Structure and properties of engineering alloys. 2nd ed. New York: McGraw-Hill; 1993.
- [8] Schuster JC, Nowotny H. Monatsh Chem 1980;111(1):113–7.
- [9] Schatt W. Intermetallische Phasen. Leipzig: VEB; 1977.
- [10] Lee BJ. Metall Trans A 1993;24(5):1017–25.
- [11] Westgren A. Jernkontorets Annaler 1933;117:501–12.
- [12] Westgren A. Jernkontorets Annaler 1935;1935:231–40.
- [13] Inoue A, Masumoto T. Scr Metall 1979;13:711–5.
- [14] Bouzy E, Bauer Grosse E, le Caer G. Philos Mag 1993;68:619–38.
- [15] Hellbom K, Westgren A. Svensk Kemisk Tidskrift 1933;45:141–50.
- [16] Bouchaud JP. Nature 1966;212:248–50.
- [17] Bouchaud JP. Ann Chim 1967;2:353–66.
- [18] Benz R, Elliott JF, Chipman J. Metall Trans 1973;4:1449–52.
- [19] Zandbergen HW, Andersen SJ, Jansen J. Science 1997;277(5330):1221–5.
- [20] Jansen J, Tang D, Zandbergen HW, Schenk H. Acta Cryst A 1998;54:91.
- [21] Vissers R, Van Huis MA, Jansen J, Zandbergen HW, Marioara CD, Andersen SJ. Acta Mater 2007;55(11):3815–23.
- [22] Hull AW. Phys Rev 1917;10:661–96.
- [23] Powder diffraction program library, Daresbury Laboratory, Warrington, UK.
- [24] Tanaka M, Sekii H, Nagasawa T. Acta Cryst 1983;A39:825–37.
- [25] International tables for crystallography 2006, vol. A: Space-group symmetry. <http://dx.doi.org/10.1107/97809553602060000100>.
- [26] Shimura S. Proc Jpn Acad 1930;6:269–71.
- [27] Glazer M, Burns G. Space groups for solid state scientists. New York: Academic Press; 2013.
- [28] Fang CM, van Huis MA, Sluiter MHF, Zandbergen HW. Phys Rev Lett 2010;105:055503.
- [29] Fang CM, van Huis MA, Sluiter MHF, Zandbergen HW. Acta Mater 2010;58:2968.
- [30] Fang CM, van Huis MA, Zandbergen HW. Scr Mater 2011;64:296–9.
- [31] Fang CM, van Huis MA, Zandbergen HW. Scr Mater 2011;63:418–21.
- [32] Kresse G, Hafner J. Phys Rev B 1994;49:14251.
- [33] Blöchl PE. Phys Rev B 1994;50:17953.
- [34] Kresse G, Furthmüller J. Phys Rev B 1999;54:1758.
- [35] Perdew JP, Burke K, Ernzerhof M. Phys Rev Lett 1996;77:3865–8.
- [36] Monkhorst HJ, Pack JD. Phys Rev B 1976;13:5188.
- [37] Jiang C, Uberuaga BP, Srinivasan SG. Acta Mater 2008;56(13):3236–44.
- [38] Tirumalasetty GK, Fang CM, Xu Q, Jansen J, Sietsma J, van Huis MA, et al. Acta Mater 2012;60:7160–8.
- [39] Zener C. J Appl Phys 1951;22:372.
- [40] Tabor D. The hardness of metals. Oxford: Oxford University Press; 2000.